

Dynamic Lithium-Ion Battery Model for System Simulation

Lijun Gao, Shengyi Liu, *Member, IEEE*, and Roger A. Dougal, *Senior Member, IEEE*

Abstract—We present here a complete dynamic model of a lithium ion battery that is suitable for virtual-prototyping of portable battery-powered systems. The model accounts for nonlinear equilibrium potentials, rate- and temperature-dependencies, thermal effects and response to transient power demand. The model is based on publicly available data such as the manufacturers' data sheets. The Sony US18650 is used as an example. The model output agrees both with manufacturer's data and with experimental results. The model can be easily modified to fit data from different batteries and can be extended for wide dynamic ranges of different temperatures and current rates.

Index Terms—Dynamic model, lithium-ion battery, rate-dependent capacity, resistive-companion, thermal model, transient response, virtual Test Bed.

NOMENCLATURE

A	Battery external surface area (m^2).
C	Capacitance (F).
c_k	Coefficient for the k th order term for the polynomial.
c_p	Specific heat (J/kgK).
E	Battery equilibrium potential (V).
$\Delta E(T)$	Temperature correction of the potential (V).
h_c	Heat transfer coefficient ($\text{W/m}^2\text{K}$).
i	Battery current (A).
i_r	Reference current (A).
m	Battery mass (kg).
n	Index number.
Q_r	Reference battery capacity (Ah).
R_1, R_2	Resistance (Ω).
R_{int}	Battery internal resistance (Ω).
SOD	State of discharge.
T	Battery temperature (K).
T_a	Ambient temperature (K).
t	Independent variable time (s).
v	Battery voltage (V).
α	Rate factor.
β	Temperature factor.

I. INTRODUCTION

BECAUSE of their high energy densities and long lifetimes, lithium-ion batteries or lithium-polymer batteries are increasingly used in systems such as portable electronics [1], electric vehicles [2]–[4], space and aircraft power systems [5] and even stationary power storage [6]–[8]. Optimizing the design of such systems requires evaluation of virtual prototypes in some computational environment. While detailed physics-based models have been built to study the internal dynamics of these batteries [9]–[14], these models are generally not suitable for system-level design exercises. On the other hand, simple dynamic models based on capacitor/resistor networks [15], [16] that can be used in a circuit simulator are generally so simplified that they lack interesting features such as nonlinear equilibrium potential, rate-dependent capacity and temperature effects. Although nonlinear phenomena can be included in circuit-based models, it dramatically increases the complexity of the modeling process. The model presented in this paper seeks an intermediate approach. On one hand, we seek sufficient accuracy to capture the major electrical and thermal properties of the battery, while on the other hand, we wish to avoid detailed calculations of internal electrochemical processes. The model is coded according to the resistive companion method [17], [18], which allows systematic handling of nonlinearities in the model equations and easy connection to other objects in a system-level simulation. The model can be easily updated to represent new varieties of batteries or a wider dynamic range than the current valid range. The model was tested in the Virtual Test Bed [19] computational environment.

In the following, we will first describe the battery model in terms of its circuit representation, mathematical equations and its implementation in resistive-companion format. Then we will show that important features of the battery model, such as nonlinear equilibrium potential, rate and temperature dependences, thermal characteristics and first-order transient response, match experimental results.

II. MODEL FORMULATION

Our objective is to replicate the electrical and thermal properties of the battery as it interacts with the external world. At this level, we approximate all electrochemical and electrothermal processes as uniform throughout the entire battery and ignore all spatial variations of concentrations, phase distributions and potentials. These assumptions allow the battery to be modeled by “bulk” parameters extracted from the experimental data, as will be discussed below.

Manuscript received January 15, 2002; revised June 13, 2002. This work was supported by the U.S. Army Communications and Electronics Command under Contract NRO-00-C-0134. This work was recommended for publication by Associate Editor A. Deutsch upon evaluation of the reviewers' comments.

The authors are with the Department of Electrical Engineering, University of South Carolina, Columbia, SC 29208 USA (e-mail: lius@enr.sc.edu).

Digital Object Identifier 10.1109/TCAPT.2002.803653

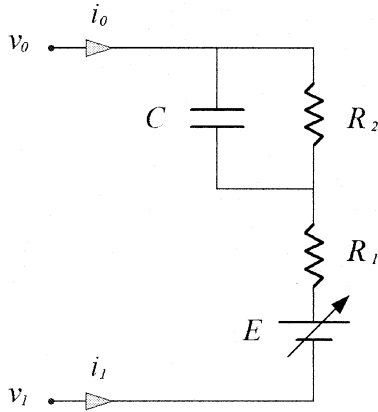


Fig. 1. Equivalent circuit representation of lithium-ion battery.

The most readily available data, whether from manufacturers' data sheets or independent measurements, are the curves of terminal voltage during constant-current discharge at constant temperature. A second set of relevant data are the voltage following a step change of current.

To fit all of these data, the model has three components:

- 1) an equilibrium potential E ;
- 2) an internal resistance R_{int} having two components R_1 and R_2 ;
- 3) and an effective capacitance that characterizes the transient response of charge double layers in the porous electrodes.

The electrical schematic of these components is shown in Fig. 1. The roles of these components and the mathematical relations that describe each are explained next.

A. Description of the Equilibrium Potential

The equilibrium potential of the battery (open-circuit voltage) depends on the temperature and the amount of active material available in the electrodes, which can be specified in terms of state of discharge (SOD). The discharge capacity of the battery depends on the discharge rate and the temperature [20], [21]. Thus, we seek a general expression for the potential $E(i, T, t)$.

A 4-step procedure is used to model the equilibrium potential based on experimental data.

- 1) First, a typical curve of battery voltage versus the depth of discharge is chosen as a reference curve. The reference curve can be arbitrarily chosen, but we suggest using a curve near the median expected operating condition, usually at the 1-C or 0.5-C rate, to yield the highest overall accuracy. The equilibrium potential as a function of the state of discharge is found by excluding the internal potential losses due to ohmic-limitation, kinetic-limitation, and concentration-limitation resistances. An n th-order polynomial is fitted to that curve.
- 2) Secondly, the discharge rate (i.e., the current) for the reference curve is chosen as the reference rate. The dependence of the state of discharge on rate is then accounted for by a rate factor $\alpha(i)$, which has value unity for the reference curve.
- 3) Thirdly, the temperature for the reference curve is chosen as the reference temperature. The dependence of the state

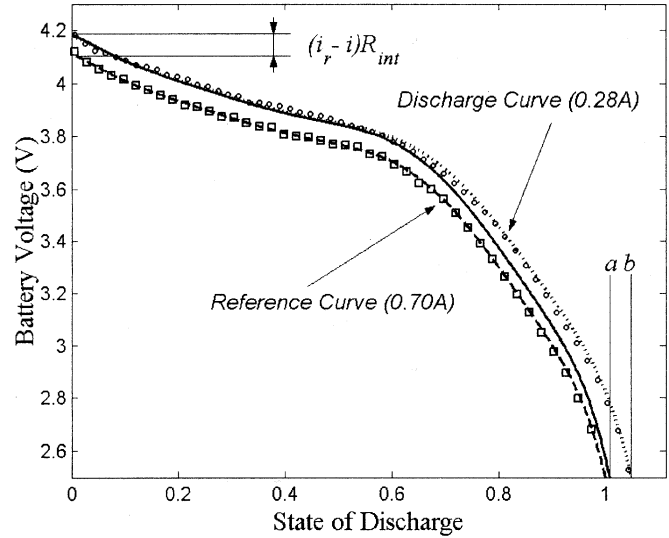


Fig. 2. Determination of the rate factor for discharge current i with respect to the reference curve at discharge rate i_r .

of discharge on temperature is accounted for by a temperature factor $\beta(T)$, which has value unity for the reference curve.

- 4) In the fourth and final step, a potential correction term $\Delta E(T)$ is used to compensate for the variation of equilibrium potential that is induced by temperature changes at the reference rate. $\Delta E(T)$ is zero at the reference temperature.

The expressions for the potential, the terminal voltage and the state of discharge, based on the above descriptions, can then be given by

$$E[i(t), T(t), t] = v[i(t), T(t), t] - R_{int}i(t) \quad (1)$$

$$v[i(t), T(t), t] = \sum_{k=0}^n c_k \cdot SOD^k[i(t), T(t), t] + \Delta E(T) \quad (2)$$

$$SOD[i(t), T(t), t] = \frac{1}{Q_r} \int_0^t \alpha[i(t)] \cdot \beta[T(t)] \cdot i(t) dt \quad (3)$$

where c_k is the coefficient of the k th order term in the polynomial representation of the reference curve and Q_r is the battery capacity referred to the cutoff voltage for the reference curve. For $k = 0$, $E = c_0$ is the open-circuit voltage at the beginning of discharge at the reference temperature for the reference curve.

The method to determine the rate factor for a discharge curve is illustrated in Fig. 2, where data from a Sony18650 lithium ion battery are used. The reference curve, indicated by squares and corresponding to experimental data for 0.7 A discharge rate, has unit discharge capacity (with respect to a cutoff voltage of 2.5 V). The polynomial fitted to the reference curve is shown by the dashed line. The curve for which the rate factor is to be found is shown by circles and corresponds to experimental data for a 0.28 A discharge rate. This curve has a larger discharge capacity equal to b . The solid line shown on the graph was obtained by removing the excess internal loss from the reference curve (i.e., moving the dashed curve upward a distance equal to $R_{int}(i_r -$

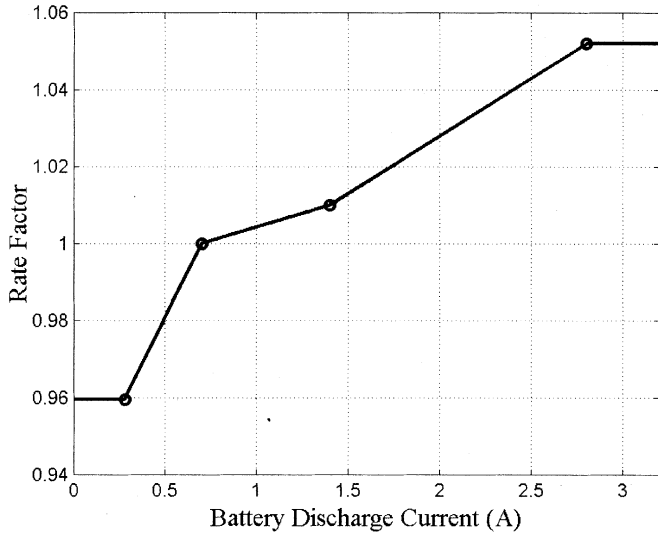


Fig. 3. Rate factor α for the lithium-ion battery (Sony US18650). The reference current is 0.7 A, corresponding to a 0.5C rate.

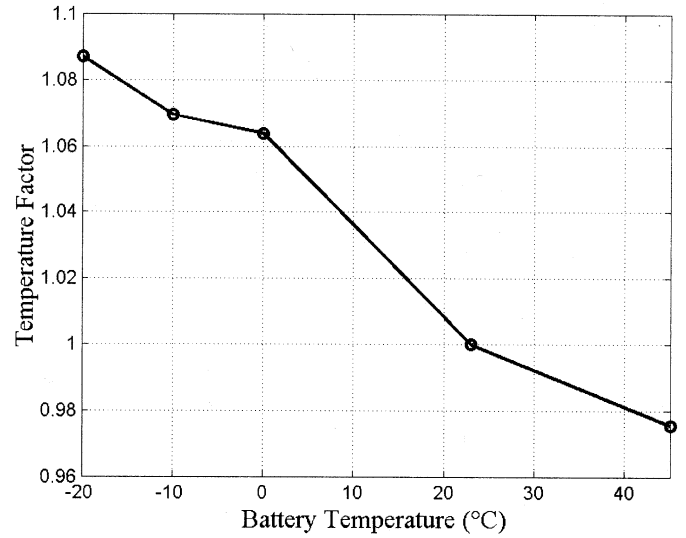


Fig. 5. Temperature factor β for the lithium-ion battery (Sony US18650). The reference temperature is 23 °C.

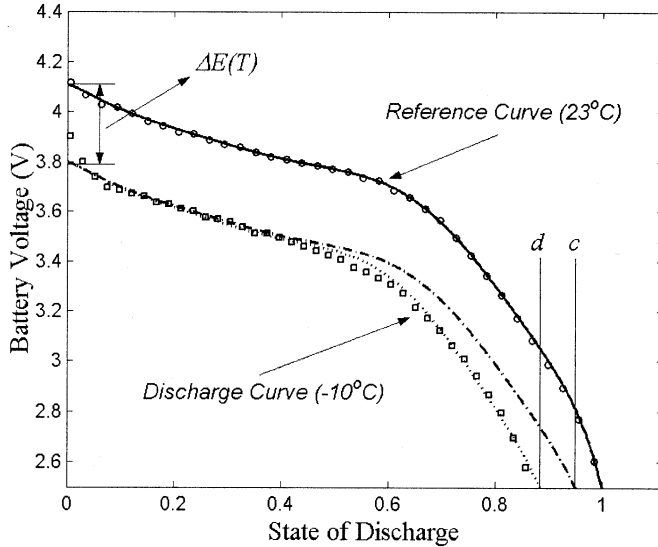


Fig. 4. Determination of the temperature factor and the temperature-dependent potential-correction term.

i), where i_r is the discharge current of the reference curve and i is the current for which the new rate factor is sought). Notice that the solid line has a discharge capacity equal to a , which otherwise would be equal to 1 if the discharge capacity were independent of the rate. Since a and b vary from curve to curve, the rate factor is, in general, defined as

$$\alpha(i) = \frac{a}{b}. \quad (4)$$

For the 0.28 A discharge rate, we find $a = 1.005$, $b = 1.046$ and $\alpha = 0.96$. The dotted line, obtained by considering both the internal loss and the rate factor, agrees with the measured data very well. Finding α for additional discharge rates produces the data shown in Fig. 3.

The temperature factors and the temperature-dependent potential-correction terms can be found by following similar procedures, as illustrated in Fig. 4. In this case, the data correspond to only one discharge rate (the reference rate, 0.7 A), but are

taken at different constant temperatures. The reference curve at the reference temperature (23°C) is shown by circles and the polynomial fit to it is shown by the solid line. The reference curve again has unit discharge capacity. The curve for which the temperature factor is sought is indicated by squares (−10°C). Its discharge capacity is d . The dot-dashed line is obtained by moving the solid line (reference curve) downward to achieve a best fit in the flat portion of the discharge curve. The distance moved is defined as the temperature correction term $\Delta E(T)$. The discharge capacity is c . The temperature factor is defined as

$$\beta(i) = \frac{c}{d}. \quad (5)$$

For the data shown in Fig. 4, $\Delta E(T) = -0.32$ V, $c = 0.949$, $d = 0.883$ and $\beta = 1.075$ for the −10°C discharge curve. The dotted line, generated by the model that considers both the temperature factor and the potential correction, has a good match with the experimental data (squares). Repeating for additional curves yields temperature factors and correction terms as shown in Figs. 5 and 6.

The definitions of the rate factor $\alpha(i)$, the temperature factor $\beta(T)$ and the temperature-dependent potential-correction term $\Delta E(T)$ are general enough that the method can be used to model a variety of battery types. Though $\alpha(i)$, $\beta(T)$ and $\Delta E(T)$ are obtained from constant-current and constant-temperature curves, we wish to use these three functions for the general case of time-varying current $i(t)$ and temperature $T(t)$, as indicated by (1)–(3). This is accomplished in the model by linearly interpolating between values for α , β and ΔE . It should be noted that the rate dependence of the battery charge process differs from that of discharge process. We found that a constant factor of $\alpha = 0.93$ for all current levels can fit the charging data very well, as will be described later.

B. Description of Potential Losses

Losses in a battery system arise primarily from the ohmic resistance due to finite conductivities of electrodes and sepa-

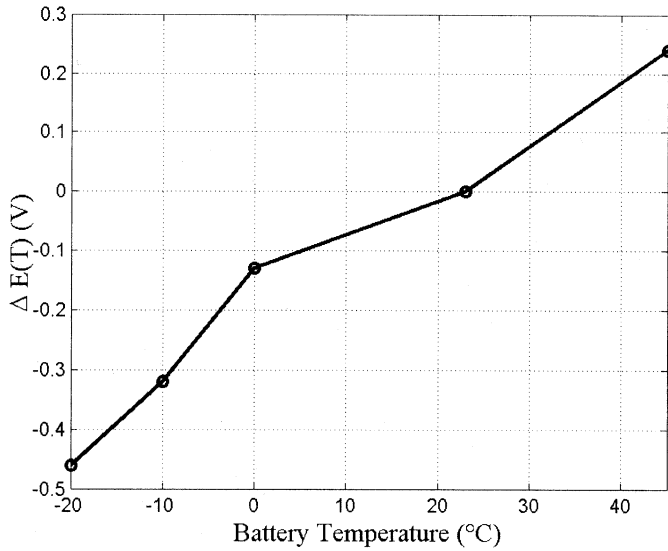


Fig. 6. Temperature-dependent potential-correction term for the lithium-ion battery (Sony US18650). The reference temperature is 23 °C.

rators, from concentration gradients of ionic species near the electrodes and from limited reaction rates (kinetics) at the electrode surfaces [22], [23]. The magnitude of each loss component depends on the particular battery chemistry, on design parameters such as geometry, pore structure and materials of electrodes and electrolytes and on temperature and discharge rate. In the present model, for Sony US18650 (or Panasonic CGR18650, or PolyStor PSC340 848-1200), within the range of interest, we have found it sufficient to lump all losses together to model them by an effective resistance. The total effective resistance can be estimated from a manufacturer's data sheet or obtained experimentally. We divide the effective resistance into two parts, R_1 and R_2 . We do not attempt to strictly trace of the origins of these resistances, but focus instead on representing the observed battery behavior. Overall, the two-resistor (R_1 and R_2) modeling approach yields a simple circuit structure that captures the major features of the battery performance. The separation of R_2 from total resistance makes it possible to incorporate the effective capacitance into model to better follow transient processes, as will be described next.

C. Description of the Transient Response

Many battery applications include stepwise or pulsed loads for which the transient response is important. We are particularly interested in applications involving parallel configurations of supercapacitors and batteries in which the effective capacitance of the battery is not insignificant. Capacitive effects arise from double-layer formation at the electrode/solution interface [24], which include capacitance due to purely electrical polarization and capacitance from diffusion limited space charges (pseudo-capacitance [25]). Both double layer capacitance and diffusion capacitance (pseudo capacitance) influence the transient response of the battery, especially when the rates of reactions are high. So we model the effects using a single lumped capacitance in parallel with the resistance R_2 . Additional details of the transient dynamics could be accounted for by using

a higher-order RC network, but for the systems considered in our work, the single capacitance was sufficient.

The fraction of the total battery resistance that is assigned to R_2 and the effective capacitance C , are found by fitting to measured data of battery transients as will be described subsequently. For the Sony US18650 and PolyStor PSC340 848-1200 batteries $R_2 = 40 \text{ m}\Omega$, $C = 4 \text{ F}$ best fit the experimental data. The total internal resistance is about 150 mΩ.

Combining the electrochemical characteristics represented by (1) to (3), with the equations for the circuit elements and the circuit constraint equations yields the following additional equation that relates the terminal potential to the terminal current

$$i(t) = \frac{1}{R_2} [v(t) - E[i(t), T(t), t] - R_1 i(t)] + C \frac{d}{dt} [v(t) - E[i(t), T(t), t] - R_1 i(t)]. \quad (6)$$

D. Description of the Thermal Characteristics

Since the equilibrium potential of the battery is temperature-dependent, the temperature must be resolved dynamically so that it is available for computation of the potential during each time step. The temperature change of the battery is governed by the thermal energy balance [26] described by

$$m \cdot c_p \cdot \frac{dT(t)}{dt} = i(t)^2 \cdot R_1 + \frac{1}{R_2} [v(t) - E[i(t), T(t), t] - i(t)R_1]^2 - h_c A [T(t) - T_a]. \quad (7)$$

The heat power terms include resistive heating and heat exchange to the surroundings. Heat generation due to entropy change or phase change, changes in the heat capacity and mixing have all been ignored without apparent loss of model accuracy, as will be shown in the next section.

E. Resistive-Companion Implementation

Equations (1)–(3), (6), and (7) are self-consistent and complete descriptions of the battery. In these equations, the battery voltage and the temperature are the “across variables” that are subject to network laws when the battery interacts with its electrical and thermal surroundings, while the equilibrium potential and the state of discharge are internal variables. To construct the model in Resistive-Companion form, the above equations were discretized following appropriate numeric algorithms as given in references [17], [18], to yield expressions for the through variables (current at electrical terminals and the heat power flow at the thermal terminal) in terms of the across variables. Since the across variables are found by the network solver for each time step, the internal state variables such as potential or state of discharge can then be determined according to the physical constraints given by (1)–(3), (6), and (7). A detailed example of resistive-companion implementation of electrochemical and thermal processes in a battery can be found in reference [27].

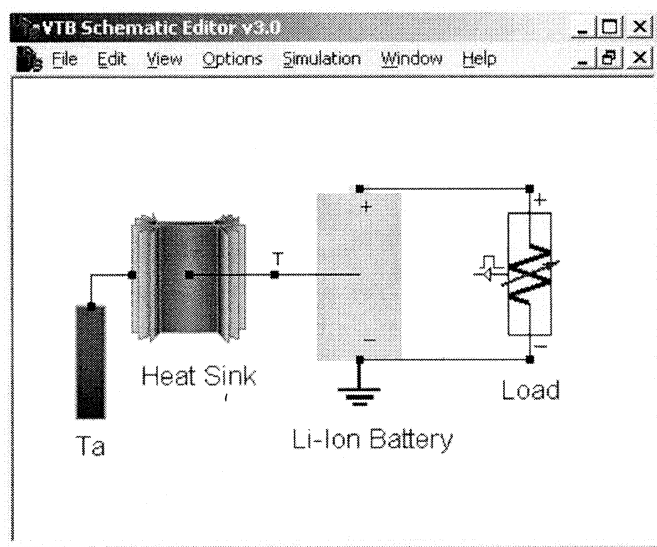


Fig. 7. Circuit for validating the battery model. The battery is discharged through a constant current load, while heat energy is transferred rapidly to the ambient.

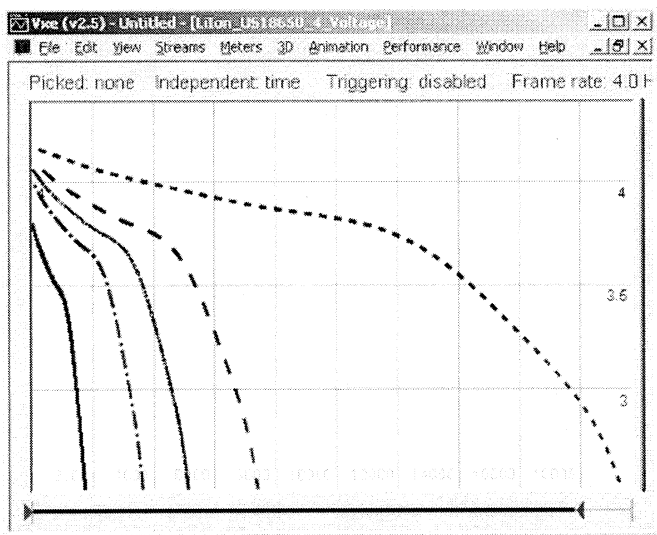


Fig. 8. Simulation results: the battery voltage (V) as a function of time (s) for constant discharge currents of (from bottom to top) 2.8 A, 1.4 A, 1.0 A, 0.7 A, and 0.28 A.

III. SIMULATION OF BATTERY CHARACTERISTICS

A dynamic model of the Sony US18650 lithium-ion battery based on the methodology given above was constructed for use in the VTB system simulation software. We will next summarize some of the major static and dynamic features of the battery model and validate the model by comparing the simulation results to the experimental data.

A. Discharge Characteristics

1) *i*-Dependence: The rate dependence of the potential was validated by testing the model in the circuit shown in Fig. 7; here the VTB schematic shows the battery connected to a programmable load that is set as a constant-current load. The initial *SOD* is set to 0. The battery is maintained at room temperature (23°C) by setting a large cooling coefficient in the heat sink, so

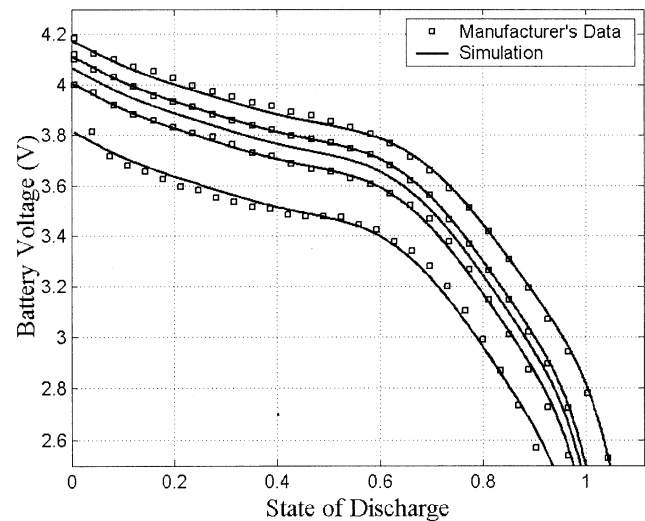


Fig. 9. Rate dependence of the battery voltage for currents of (from top to bottom) 0.28 A, 0.7 A, 1.0 A, 1.4 A, and 2.8 A at a constant temperature of 23 °C.

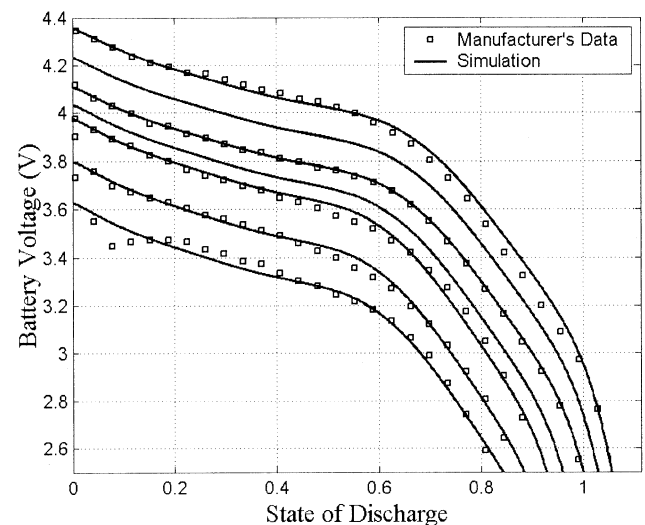


Fig. 10. Battery voltage versus *SOD*, at temperatures of (top to bottom) 45 °C, 34 °C, 23 °C, 10 °C, 0 °C, -10 °C, and -20 °C. The discharge rate is 0.7 A.

that the heat generated in the battery can be quickly transferred to the ambient. This simulates the idealized constant-temperature case for which manufacturer's data are usually given. The results of discharge tests at 2.8 A, 1.4 A, 1.0 A, 0.7 A, and 0.28 A are shown in Fig. 8.

The data shown in Fig. 8 were compared to manufacturer's data by converting through the relations between voltage and state of discharge. Fig. 9 shows the resulting rate dependence of the potential. As expected, a near perfect match between the model and the experimental results was obtained for the reference curve (0.7 A, 0.5C rate) and good agreement is also obtained for all rates from 0.2C to 2.0C. Notice that the capacity is 1.0 for the reference rate, but is larger or smaller when the discharge current differs from the reference rate. Notice also that this graph contains a curve corresponding to a 1 A discharge rate that was not available from the manufacturers data but that was automatically computed using data interpolated from Fig. 4.

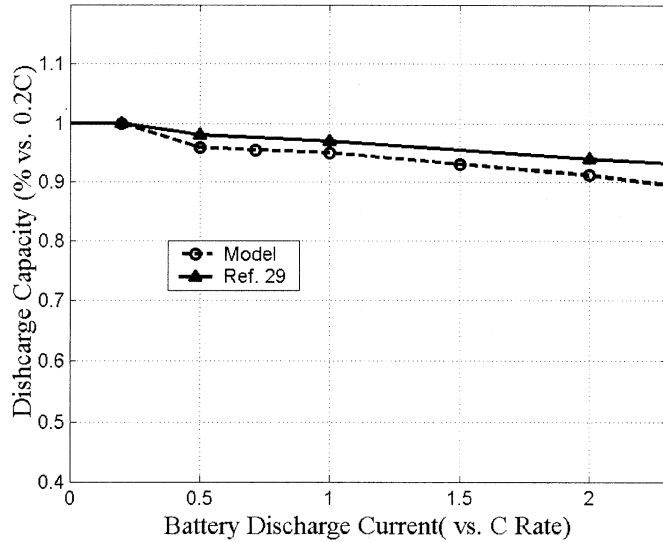


Fig. 11. Comparison of discharge capacities of Sony lithium ion batteries obtained from the model (circles) and the experimental data (triangles, [29]).

2) *T-Dependence*: To validate the temperature dependent characteristics of the battery model the circuit of Fig. 7 was used again, this time with the load set to draw a constant current of 0.7 A, but with the environmental temperature set to various values. The battery was then discharged repeatedly from full charge to a cutoff voltage (2.5 V) at each temperature. Again, the battery temperature was maintained constant by setting the cooling coefficient large enough so that any heat generated internally was nearly instantly transferred to the ambient. The simulation data were processed to obtain the relation between the voltage and the state of discharge and compared to the manufacturer's data. An excellent match was achieved, as shown in Fig. 10, for the reference temperature (23°C), along with good agreement throughout the range from -20°C to 45°C . The graph contains two curves generated by the model that were not available in the experimental data.

As can be noticed from Figs. 9 and 10, there is some disagreement between experiment and model. In particular, the curve in Fig. 10 for the discharge at -20°C behaves in a complex manner that is not seen for temperatures above 0°C —the voltage dips down at the beginning of discharge and then recovers at about 0.2 SOD for a 1.0C discharge. At low temperatures, the surface kinetic potential loss becomes important due to several processes such as precipitation, dissolution, desorption and adsorption that affect the reaction kinetics. As a result, our constant resistance approximation does not prevail [28]. Similar deviations, though to a lesser extent, can be found for high current discharge (the curve for 2.0C discharge in Fig. 9). At high reaction rates, both the surface kinetics and concentration limitation are significant. In addition, the battery becomes not isothermal so our lumped element model is less appropriate. These inadequacies will be addressed in future improvements to the model.

3) *Discharge Capacity*: Discharge capacity can be obtained for different discharge rates at a given temperature according to (4). These are plotted in Fig. 11 and compared against the discharge capacity of a Sony lithium ion polymer battery (Sony's gel polymer electrolyte) [29]. The Lithium ion polymer battery

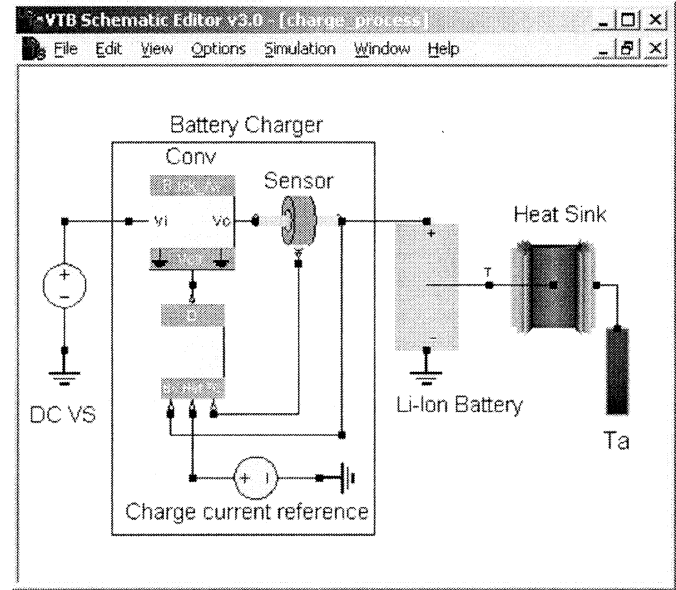


Fig. 12. VTB schematic view of the circuit for simulating the battery charge characteristics.

in the cited reference was of 4.2 V OCV, 3.7 V nominal voltage and a 690 mAh nominal capacity (about a half of US18650). The data for the lithium ion polymer battery was taken at 23°C , 3.0 V cutoff and normalized to 0.2C rate. Therefore we convert the data obtained from our model to the 0.2C basis also. As can be seen from Fig. 11, two batteries behave similarly and close to each other in their discharge capacities. The small difference between them may result from variation in construction, electrode and electrolyte materials [21], [29], [30].

B. Charge Characteristics

The system shown in Fig. 12 was used to analyze the charging characteristics of the battery. Here, a DC voltage source charges the battery through a charger, which consists of a buck converter, a charge controller and voltage and current sensors. The controller enforces a conventional constant current then constant voltage charging algorithm. The current reference is set to 1.0 A by an external source. The battery charges at this current until the battery voltage reaches 4.2 V at which the charging mode changes to constant voltage and the current eventually decays to zero.

The rate dependence of the charging process is generally different from that of the discharge process. In the case of charging at 1 A or lower a constant rate factor of $\alpha = 0.93$ is used. In the model, we use 0.93 for all charging current levels. The characteristics of the charge process from both simulation and manufacturer's data are shown in Fig. 13. The simulation results fit the experimental data extremely well.

C. Thermal Characteristics

Here, we use the model to study how heat sinking of the battery affects its operation. Using the same simulation as shown in Fig. 7 with initial SOD of the battery set to 0 and the load set to draw a constant current of 1.4 A, we vary the heat transfer coefficient. Other parameters are given in Table I.

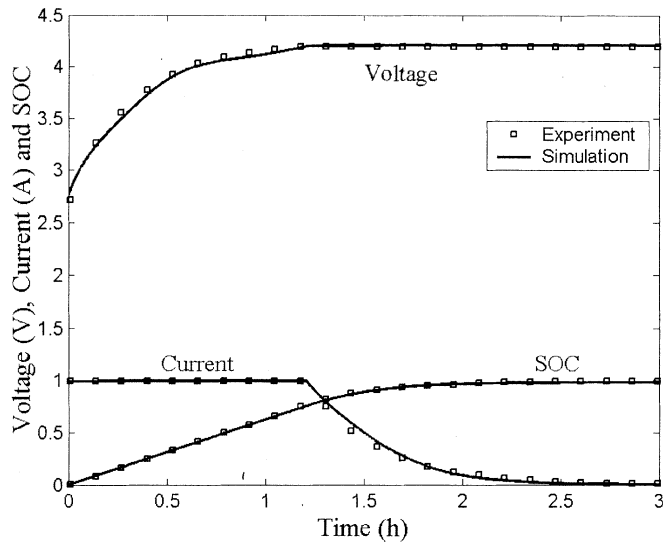


Fig. 13. Battery charge characteristics at 23°C and 1.0 A.

TABLE I
PARAMETERS FOR SIMULATION OF US 18650 BATTERY

Surface Area (m ²)	4.3E-3
Weight (g)	41
Heat capacity (J/kg /K)	925
Ambient Temperature (°C)	23

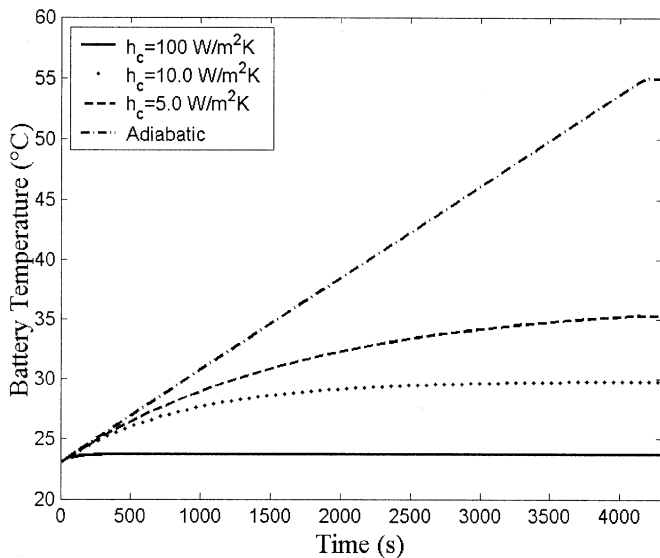


Fig. 14. Variations of the battery temperature during discharge (1.4 A, 23°C ambient) for different cooling conditions. Under adiabatic conditions, the battery is fully depleted at about 4200 s.

Fig. 14 shows the variation of the battery temperature during discharge for different cooling conditions. Notice that the final temperatures are 30°C and 35°C respectively for the constant cooling coefficients of 10 W/m²/K and 5 W/m²/K. Under adiabatic conditions, the battery temperature increases almost linearly until the end of discharge, at which time it has reached

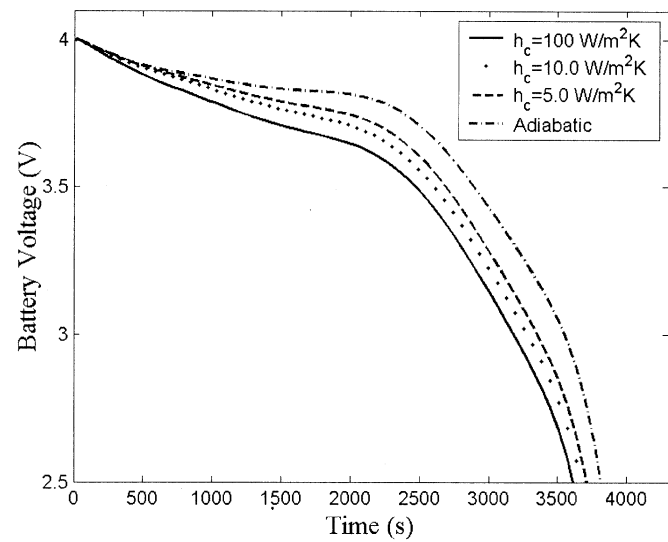


Fig. 15. Battery voltage under different cooling conditions.

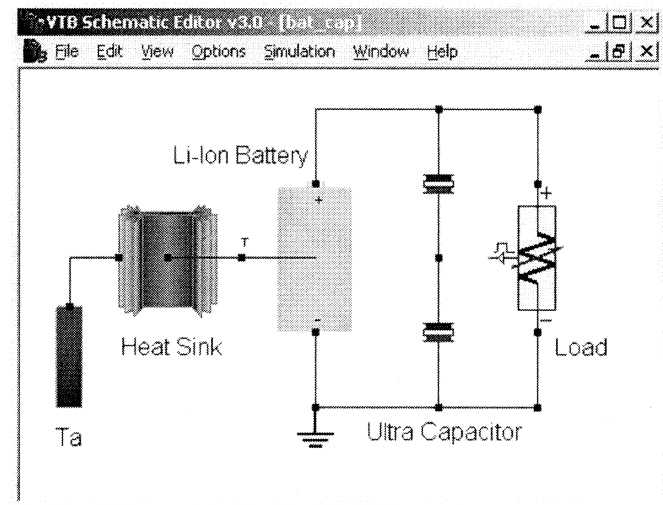


Fig. 16. VTB Simulation of battery-capacitor hybrid power source.

55°C. The battery temperature is nearly equal to the ambient (23°C) for very large cooling coefficients.

Battery voltage during discharge is a function of the heat transfer conditions, as shown in Fig. 15. Here the battery temperature depends on the cooling coefficient and this higher temperature impacts the terminal voltage. It can be seen that higher operating temperatures yield larger relative capacities and higher terminal voltages. (But of course battery life is adversely affected by high temperatures, but is not predicted by this model.)

D. Transient Response

When a battery is operated in pulse mode, the double layer capacitance of the electrodes significantly affects the overall impedance. The R_2/C network included in the model captures the first order transient response of the battery, as described earlier. Validation of this aspect of the model was conducted by comparison to experimental data taken from tests of a battery/ultracapacitor hybrid power source configured as shown in Fig. 16. Experimentally and in simulation, the load drew a

TABLE II
HYBRID POWER SOURCE PARAMETER SETUP

Component	Model Type	Specifications
Battery	Sony US18650	1.5Ah (1 cell)
Ultracapacitor	PowerCache PC100	100F (2 cells in series)
Load	Ideal pulse current load.	$I = 4.0$ A (on), 0.0 A (off) Freq. = 0.25 Hz, Duty = 25%

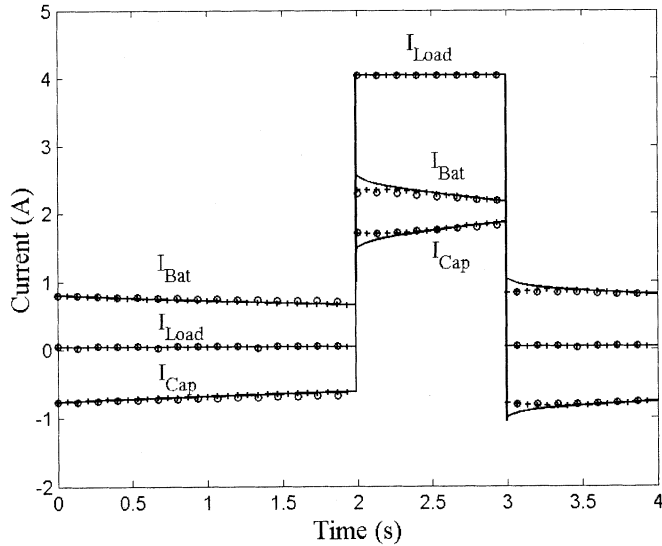


Fig. 17. Transient response of hybrid power source. Experimental data (circle), using this battery model (cross) and using battery model lacking effective capacitance (solid line).

pulsed current. The advantages of such a system are that the power and discharge life of the battery can be boosted and the overall system power density can be increased [31]. The principle of operation of the system is that the battery recharges the ultracapacitor during the pulse-off period and the ultracapacitor then augments the battery capacity during the pulse on period. This delivers a higher power to the load, with lower internal losses. The ultracapacitor model used here, based on that of Miller *et al.* [32], [33], represents the Maxwell PowerCache PC100 and was previously validated. Table II lists the system parameters.

Fig. 17 shows the battery current, the ultracapacitor current and the load current for one period (4 s) in steady state operation. Zero seconds on the time axis refers to the beginning of the data acquisition period, not the beginning of the experiment. Notice that the battery discharges (positive current) both while the load pulse is on and off, while the ultracapacitor discharges (positive current) when the load is on but charges (negative current) when the load is off. Three sets of data are shown. The experimental data are indicated by open circles. Simulation results obtained from the battery model described here are shown by crosses. Simulation results obtained from a simplified battery model that had all of the features of the current model except for capacitance are shown with the solid line. The complete battery model gave very good fidelity whereas the model that did not include the effective capacitance deviated significantly at the beginning of each load pulse.

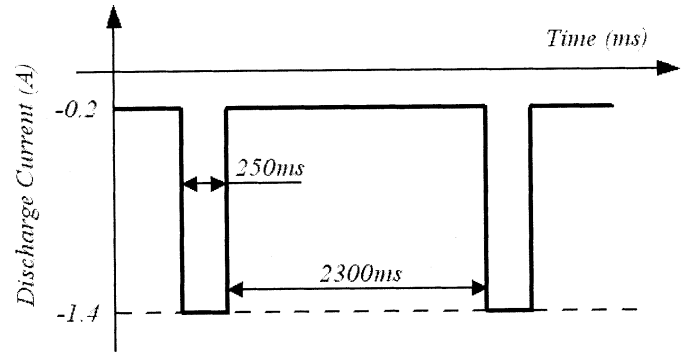


Fig. 18. Pulsed current discharge profile of CDMA.

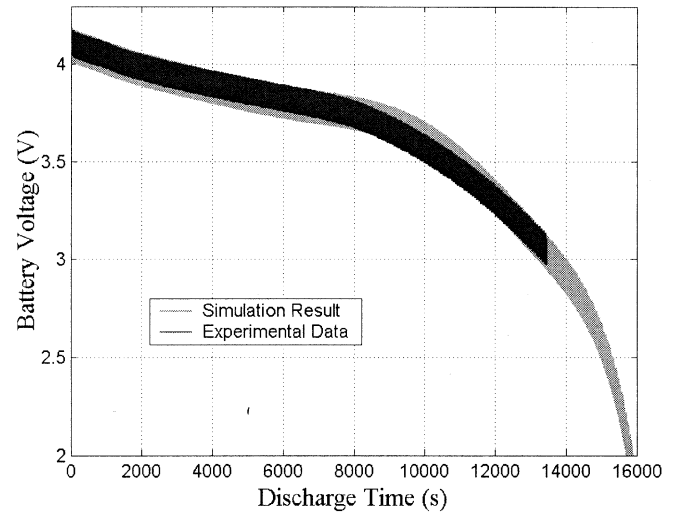


Fig. 19. CDMA discharge test for a single cell of Sony US18650 Battery. Comparison of the simulation result to the experimental data.

IV. DYNAMIC SIMULATIONS

To further validate the model, extensive dynamic simulations were conducted following some industry standards, for example, the CDMA cellular load cycle [34]. Fig. 18 shows the pulsed current discharge profile of CDMA2, in which the battery discharges at 1.4 A for 250 ms and then at 0.2 A for the rest of the 2.55 s pulse period. The battery runs until it cuts off at 2.5 V.

In Fig. 19, the simulation result for the battery voltage is presented and compared against the experimental test. The experimental data were obtained by testing a brand new US 18650 cell taken from a consumer electronics item. The pulsed current discharge mode was set up by using an electronic load and controlled by the LabView software. To protect the battery, the cut off voltage in the test was set to 3.0 V. Since the pulse rate is high and the experiment duration is in the range of hours, the pulses are compressed into bands and the details of the pulses can not be viewed. As can be seen, over the entire discharge course, the simulation result (shallow color band) and the experimental data (dark color band) agree well, though differences exist. To compare the pulse details, the experiment was repeated using faster data acquisition speed. Results are presented in Figs. 20–23.

Fig. 20 shows the voltages for the pulse between 3004.602 s and 3007.152 s. The measured and computed pulse ampli-

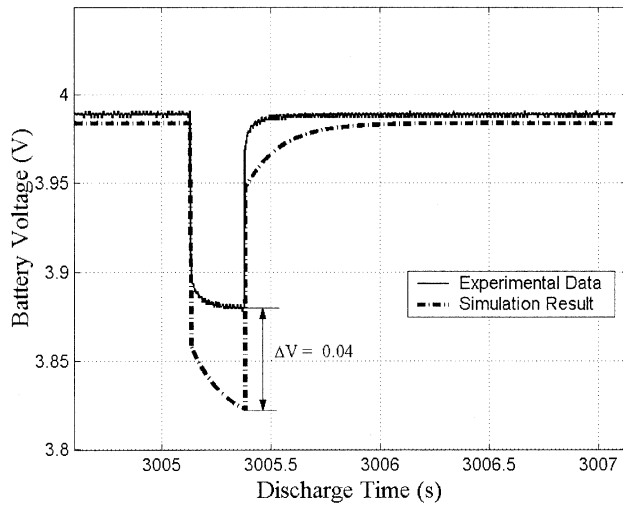


Fig. 20. Single pulse comparison for the time between 3004.602 s and 3007.152 s.

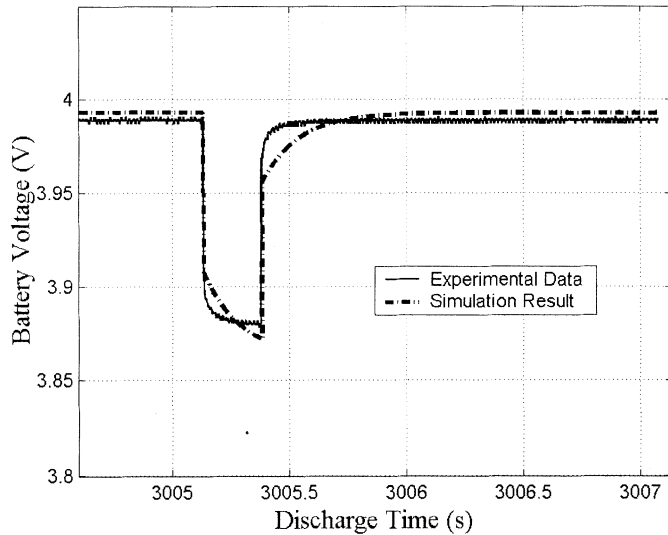


Fig. 21. Single pulse comparison for the time between 3004.602 s and 3007.152 s with $R_1 = 80 \text{ m}\Omega$, $R_2 = 40 \text{ m}\Omega$.

tudes differ by about 40 mV during the 1.4 A discharge. Like any other electronic components, the characteristics of batteries depend not only on their design, material composition and geometry, but also on many other factors, such as defects, shelving time, aging effect and service history. Therefore the characteristics may differ from one battery to another even for the same production batch. The characterization in our model was based on the manufacturer's data typical to the same type of batteries, but it may slightly differ among individual ones. Thus, the characterization shall be focused on the major features, which is fulfilled by our model. Nonetheless, it is easy to make up the difference by simply adjusting the internal resistance. Fig. 21 is the comparison result after the total internal resistance in the model was reduced to $120 \text{ m}\Omega$ (with $R_1 = 80 \text{ m}\Omega$, $R_2 = 40 \text{ m}\Omega$). As a result, a better fitting for internal loss was obtained.

Using the new values for R_1 and R_2 , the simulation results for the pulse between 7029.602 s and 7032.152 s, the pulse between 12 879.602 s and 12 882.152 s were also compared to the experimental data, as shown by Figs. 22 and 23 respectively. A

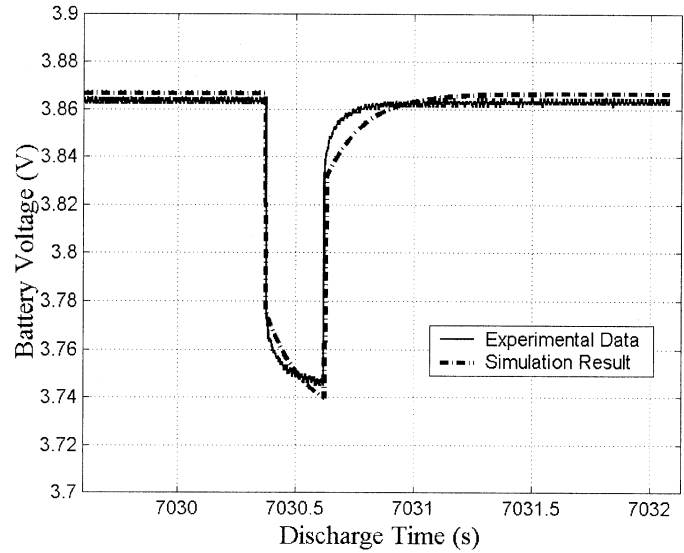


Fig. 22. Single pulse comparison for the time between 7029.602 s and 7032.152 s with $R_1 = 80 \text{ m}\Omega$, $R_2 = 40 \text{ m}\Omega$.

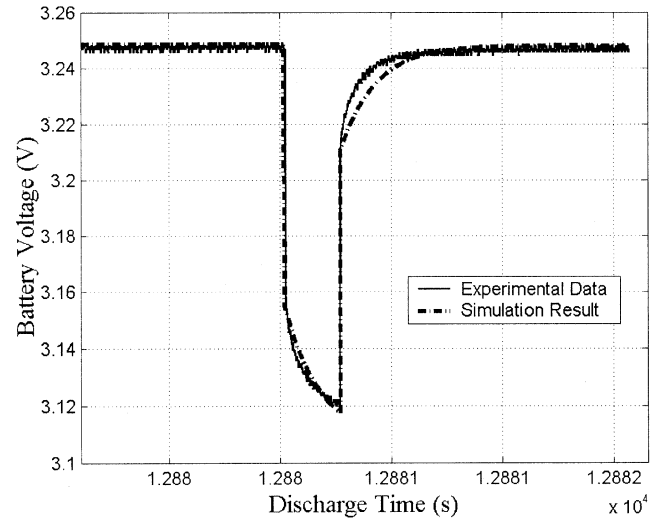


Fig. 23. Single pulse comparison for the time between 12 879.602 s and 12 882.152 s with $R_1 = 80 \text{ m}\Omega$, $R_2 = 40 \text{ m}\Omega$.

good agreement in internal resistive drop was obtained between the model and the experiment according to these comparisons. The differences shown by the transient processes (Figs. 21–23) indicate that the effective capacitance of the battery under test is smaller than that of the model and it actually varies as a function of the state of discharge. Indeed, both the double layer capacitance and the diffusion capacitance of the porous electrode are strong functions of the charge density and the thermodynamic temperature [24]. As a result, the effective capacitance increases during the course of a battery discharge. The variable capacitance effect is not included in the present version of the model, but it will be included in further model development. Fig. 24 shows the temperature of the battery for the discharge profile of CDMA2. The effective cooling coefficient was set to $6 \text{ W/m}^2/\text{K}$ (simulating natural convection cooling condition) and the initial and ambient temperature was 296 K. As can be seen, the total temperature increase is about 1.5 degree. An experimental result for the temperature was not available for comparison.

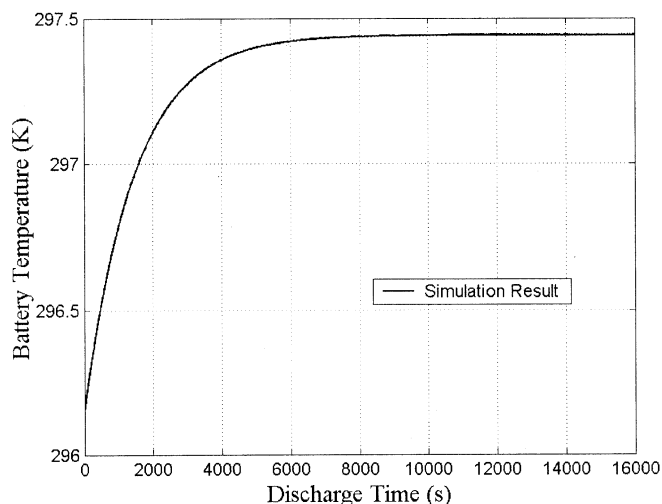


Fig. 24. Battery temperature increase for CDMA2 test.

V. CONCLUSION

We have described here a complete behavioral model of a lithium-ion battery that is suitable for portable power system studies. The model was formulated in a general sense, but was coded specifically for use in the Virtual Test Bed computational environment. The method accounts for rate- and temperature-dependence of the capacity, thermal dependence of the equilibrium potential and transient response. A 4-step modeling procedure, based on use of manufacturers' data, allows the model to have both good accuracy and the flexibility to represent different types of batteries. Construction and validation of a specific model of a Sony US18650 was described. Simulation results show that the model agrees well with experimental data in both static and dynamic characteristics.

The present model primarily uses simple representations for the potential loss and transient process modeling. This is not sufficient in all cases. The model deviates from the experimental data at low temperatures and at high discharge rates. The internal losses in these two cases are apparently the result of many intricate processes. In addition to ohmic loss, the loss due to surface kinetics becomes important at low temperature regime; while the resistances due to both the surface phenomena and the concentration limitation are also significant in the high rate regime. The effect of *SOD* and perhaps the temperature, on the transient process was also observed, which, according to the experimental data, shows an increasing effective capacitance during discharge. All these effects are not included in the present model, but they will be considered in the future model development so that the model can be applied to studies of high power systems. In addition, the present model is validated by using mostly discharge data and its validity for representing charging processes is unknown.

ACKNOWLEDGMENT

The authors wish to thank C. Holland for conducting the physical experiments to which the simulations were compared.

REFERENCES

- [1] S. Megahed and W. Ebner, "Lithium-ion battery for electronic applications," *J. Power Sources*, vol. 54, pp. 155–162, 1995.
- [2] C. Fellner and J. Newman, "High-power batteries for use in hybrid vehicles," *J. Power Sources*, vol. 85, pp. 229–236, 2000.
- [3] B. Kennedy, D. Patterson, and S. Camilleri, "Use of lithium-ion batteries in electric vehicles," *J. Power Sources*, vol. 90, pp. 156–162, 2000.
- [4] T. Horiba, K. Hironaka, T. Matsumura, T. Kai, M. Koseki, and Y. Muranaka, "Manganese type lithium ion battery for pure and hybrid electric vehicles," *J. Power Sources*, vol. 97–98, pp. 719–721, 2001.
- [5] G. Bruce, P. Mardikian, and L. Marcoux, "50 to 100 Ah lithium-ion cells for aircraft and spacecraft applications," *J. Power Sources*, vol. 65, pp. 149–153, 1997.
- [6] T. Iwahori, I. Mitsuishi, S. Shiraga, N. Nakajima, H. Momose, Y. Ozaki, S. Taniguchi, H. Awata, T. Ono, and K. Takeuchi, "Development of lithium ion and lithium polymer batteries for electric vehicle and home-use load leveling system application," *Electrochem. Acta*, vol. 45, pp. 1509–1512, 2000.
- [7] M. Majima, K. Hanafusa, Y. Oka, G. Tanaka, H. Yoshida, E. Yagasaki, and T. Tada, "Development of 1 kWh (300 Ah) class lithium-ion battery," *J. Power Sources*, vol. 68, pp. 448–450, 1997.
- [8] M. Majima, S. Ujiie, E. Yagasaki, K. Koyama, and S. Inazawa, "Development of long life lithium ion battery for power storage," *J. Power Sources*, vol. 101, pp. 53–59, 2001.
- [9] M. Doyle, T. T. Fuller, and J. Newman, "Modeling of galvanostatic charge and discharge of the lithium/polymer/insertion cell," *J. Electrochem. Soc.*, vol. 140, p. 1526, 1993.
- [10] T. F. Fuller, M. Doyle, and J. Newman, "Simulation and optimization of the dual lithium ion insertion cell," *J. Electrochem. Soc.*, vol. 141, no. 1, pp. 1–10, 1994.
- [11] M. Doyle and J. Newman, "Comparison of modeling predictions with experimental data from plastic lithium ion cells," *J. Electrochem. Soc.*, vol. 143, no. 6, pp. 1890–1903, 1996.
- [12] P. Arora, M. Doyle, and R. E. White, "Mathematical modeling of the lithium deposition overcharge reaction in lithium-ion batteries using carbon-based negative electrodes," *J. Electrochem. Soc.*, vol. 146, no. 10, pp. 3543–3553, 1999.
- [13] L. Song and J. W. Evans, "Electrochemical-thermal model of lithium polymer batteries," *J. Electrochem. Soc.*, vol. 147, no. 6, pp. 2086–2095, 2000.
- [14] W. B. Gu and C. Y. Wang, "Thermal-electrochemical modeling of battery systems," *J. Electrochem. Soc.*, vol. 147, no. 8, pp. 2910–2922, 2000.
- [15] S. C. Hageman, "Simple pspice models let you simulate common battery types," *EDN*, pp. 117–132, Oct. 1993.
- [16] V. H. Johnson, A. A. Pesaran, and T. Sack, "Temperature-dependent battery models for high-power lithium-ion batteries," *Battery Thermal Manag. Assessment*, 2002.
- [17] D. A. Calahan, *Computer-Aided Network Design*, Rev. Ed. New York: McGraw-Hill, 1972.
- [18] M. R. Lightner and S. W. Director, "Computer-aided design of electronic circuits," in *Electronics Engineers' Handbook*, 3rd ed, D. G. Fink and D. Christiansen, Eds. New York: McGraw-Hill, 1989, sec. 27.
- [19] R. A. Dougal, C. W. Brice, R. O. Pettus, G. Cokkinides, and A. P. S. Meliopoulos, "Virtual prototyping of PCIM systems—The Virtual Test Bed," in *Proc. PCIM/HFPC '98 Conf.*, Santa Clara, CA, Nov. 1998, pp. 226–234.
- [20] (2000) Lithium-Ion Batteries: Individual Data Sheet CGR18650. Panasonic. [Online]. Available: <http://www.panasonic.com/industrial/battery/>
- [21] (2001) Hard Carbon Lithium Ion Rechargeable Battery. Sony. [Online]. Available: <http://www.sony.co.jp/en/Products/BAT/ION/Catalog-e.pdf>
- [22] J. S. Newman, *Electrochemical Systems*, 2nd ed. Englewood Cliffs, NJ: Prentice-Hall, 1991.
- [23] —, *Electrochemical Systems*, 2nd ed. Englewood Cliffs, NJ: Prentice-Hall, 1991.
- [24] —, *Electrochemical Systems*, 2nd ed. Englewood Cliffs, NJ: Prentice-Hall, 1991.
- [25] B. E. Conway, "Transition from 'Supercapacitor' to 'Battery' behavior in electrochemical energy storage," *J. Electrochem. Soc.*, vol. 138, no. 6, pp. 1539–1548, 1991.
- [26] D. Bernardi, E. Pawlikowski, and J. Newman, "A general energy balance for battery systems," *J. Electrochem. Soc.*, vol. 132, no. 1, pp. 5–12, 1985.
- [27] R. A. Dougal, S. Liu, L. Gao, and M. Blackwelder, "Virtual Test Bed for advanced power sources," *J. Power Sources*, 2002.

- [28] G. Nagasubramanian, R. G. Jungst, and D. H. Doughy, "Impedance, power, energy and pulse performance characteristics of small commercial Li-ion cells," *J. Power Sources*, vol. 83, pp. 193–203, 1999.
- [29] K. Kezuka, T. Hatazawa, and K. Nakajima, "The status of sony Li-ion polymer battery," *J. Power Sources*, vol. 97–98, pp. 755–757, 2001.
- [30] Y. Nishi, "Lithium ion secondary batteries; past 10 years and the future," *J. Power Sources*, vol. 100, pp. 101–106, 2001.
- [31] R. A. Dougal, S. Liu, and R. E. White, "Power and life extension of battery/ultracapacitor hybrids," *IEEE Trans. Comp. Packag. Technol.*, vol. 25, pp. 120–131, Mar. 2002.
- [32] J. R. Miller, "Battery-capacitor power source for digital communication applications: Simulations using advanced electrochemical capacitors," in *Proc. Electrochem. Soc.*, vol. 95–29, Oct. 1995, pp. 246–254.
- [33] A. F. Burke and J. R. Miller, "Test procedures for high energy density, electrochemical capacitors," in *Proc. Electrochem. Soc.*, vol. 95–29, 1995, pp. 280–297.
- [34] (2002). [Online]. Available: http://www.arbin.com/Products/GSM_CDMA/GSM.pdf.



Lijun Gao, received the B.S.E.E and M.S.E.E degrees from Shandong University, Jinan, China, in 1997 and 2000, respectively, and is currently pursuing the Ph.D. degree at the University of South Carolina, Columbia.

His recent interest is focused on modeling and simulation of hybrid electric vehicles (HEVs) and hybrid advanced power sources (HAPs).



Shengyi Liu, (M'96) received the B.Sc. and M.Sc. degrees from Tsinghua University, Beijing, China, in 1982 and 1985, respectively, and the Ph.D. degree in electrical engineering from University of South Carolina, Columbia, in 1995.

Prior to joining the Department of Electrical Engineering, University of South Carolina, as a Research Professor, he was Senior Research and Development Engineer from 1995 to 1999 at InnerLogic, Inc. Research interests include application and control study of advanced power sources and systems, modeling and simulation of interdisciplinary systems under virtual test bed computational environment. His interests also include modeling, design and applications of physical electronics-based devices, power semiconductor devices, and converters.



Roger A. Dougal (SM'94) received the Ph.D. degree in electrical engineering from Texas Tech University, Lubbock, in 1983.

He then joined the faculty at the University of South Carolina, Columbia. He is the Director of the Virtual Test Bed Project, which is developing an advanced simulation and virtual prototyping environment for multidisciplinary dynamic systems.

Dr. Dougal received the *Samuel Litman Distinguished Professor of Engineering* award and has been honored as a *Carolina Research Professor*.